International Journal of Fatigue 155 (2022) 106616

Contents lists available at ScienceDirect

International Journal of Fatigue

journal homepage: www.elsevier.com/locate/ijfatigue

In situ X-ray imaging of fatigue crack growth from multiple defects in additively manufactured AlSi10Mg alloy

Weijian Qian [a], Shengchuan Wu [a,b,*], Zhengkai Wu [a], Saad Ahmed [b], Wen Zhang [b], Guian Qian [c], Philip J. Withers [b]

[a] State Key Laboratory of Traction Power, Southwest Jiaotong University, Chengdu 610031, China
[b] Henry Royce Institute, Department of Materials, The University of Manchester, Manchester M13 9PL, UK
[c] State Key Lab. of Nonlinear Mechanics, Institute of Mechanics, Chinese Academy of Sciences, Beijing, 100190, China

ARTICLE INFO

Keywords:
Additive manufacturing (AM)
Multiple defects
Synchrotron X-ray micro computed tomography (μCT)
Fatigue crack growth prediction
AlSi10Mg alloys

ABSTRACT

Defects introduced during additive manufacturing currently control fatigue resistance and lead to a large scatter in lifetime, with pancake shaped lack of fusion (LOF) defects being particularly potent. In this study the fatigue crack propagation life of selective laser-melted (SLM) AlSi10Mg alloy is considered in cases where single cracks and multiple cracks can initiate from LOF defects under high cycle fatigue (HCF). Firstly, the aspect ratios of initially long fatigue cracks were determined for critical LOF defects obtained from X-ray CT renderings using the critical defect regularization method, and the response surface method used to obtain the stress intensity factor of the crack front quickly and continuously. Then a single crack propagation model considering the evolution of the crack aspect ratio established to predict the crack propagation life which is in good agreement within *in situ* X-ray CT imaging of the crack front when a single crack is dominant. The crack propagation phase was predicted to represent 35–60% of the total fatigue life representing a larger fraction at high stress amplitudes. Multiple cracks were found to initiate cracks at the larger stress amplitudes. In cases where multiple cracks arise this is non-conservative and so a synergistic multiple fatigue crack growth (smFCG) model was developed based on multiple defects measured a priori by X-ray CT to depict the competitive cracking effect. Compared with the single crack model, the smFCG model predicts a shorter propagation life (by 5–10%) when multiple defects are involved since it considers all the initial defects within the crack initiation region. Given the propensity of large numbers of defects in AM material this approach may be more appropriate in many cases.

1. Introduction

As a popular additive manufacturing (AM) technology, selective laser melting (SLM) can produce complex three-dimensional metal components with low porosity [1,2] offering significant advantages over classical processing methods [3]. Given the extremely light weight of Al alloys, geometrically complex Al alloy components based on SLM are finding increasing application in the aerospace and military sectors [3,4]. By optimizing the SLM parameters and microstructures, static mechanical properties similar to those obtained by casting and forging can be achieved [1,2,5]. However residual stress [6], surface roughness [7], and internal defects [8,9] can deleteriously affect the fatigue resistance of SLM parts. Of these entrained defects are currently the most important factor in controlling the fatigue life of SLM-processed Ti [10,11] and Al [12–14] alloys.

A significant body of work has focused on the experimental and theoretical analysis of the effect of defects on the fatigue life of additively manufactured parts. Tammas Williams et al. [15] were the first to monitor the growth of cracks from defects of additively manufactured Ti alloys by time-lapse X-ray computed tomography (CT). They found that near surface defects were much more likely to nucleate critical crack growth than similarly sized (in terms of Murakami's $\sqrt{\text{area}}$ parameter) internal defects and that the scatter in cycles to failure could largely be rationalized in terms of the size of the critical defects [15]. Larossa et al. [16] found that fatigue life of additively manufactured parts tested perpendicular to the build direction to be higher than those tested parallel to it. This has been shown to be because the pancake-like lack of fusion (LOF) defects present a more potent threat for this testing direction [17]. Hu et al. [11] have shown than an extended Kitagawa-Takahashi fatigue diagram can be used to provide a framework for

* Corresponding author at: State Key Laboratory of Traction Power, Southwest Jiaotong University, Chengdu 610031, China.
E-mail address: wusc@swjtu.edu.cn (S. Wu).

https://doi.org/10.1016/j.ijfatigue.2021.106616
Received 17 August 2021; Received in revised form 7 October 2021; Accepted 16 October 2021
Available online 21 October 2021

defect-tolerant design, which includes a classical safe-life region and a defect-determined lifetime in the finite life region on the basis of a single critical defect.

The problem of multiple fatigue cracks has attracted attention because of its frequent occurrence in aircraft structures [18]. Pang et al. [19] proposed a crack coalescence model for predicting the relatively reliable fatigue life of cast alloys. The stable growth of long cracks is accomplished by the merging of adjacent cracks or defects instead of the propagation of an individual crack [20,21]. Murakami et al. [22] calculated the stress intensity factor (SIF) of two coupled surface cracks; however, this analytical solution was dependent on the unique crack morphology. Sethuraman et al. [23] proposed an empirical equation for evaluating crack interaction using SIF results calculated by the finite element (FE) method. Kishimoto et al. [24] proposed a no-interaction and immediate transition (NIIT) method to simplify the treatment of the coupling effect of multiple cracks. In addition, a similar crack coalescence criterion also can be found in BS 7910 (UK guidelines for acceptance assessment methods for metal structures containing defects).

Despite the propensity for AM parts to contain a large number of defects, few studies have assessed the effect of multiple cracks or defects on their fatigue life. In the current paper, a synergistic multiple fatigue crack growth (smFCG) model is proposed within the framework of fracture mechanics based on the *in situ* observation of crack-nucleating defects by advanced X-ray CT. The initial fatigue crack length is defined by the circumscribed semi-ellipse of the critical LOF defect inside the SLM-processed AlSi10Mg alloy. The fatigue crack growth characteristics described by the classical NASGRO equation [25] provide the basis of crack growth life evaluation. Based on the existing research, the response surfaces of the crack front geometry correction factor are constructed to quickly calculate the crack growth driving force. The NIIT method is then used to deal with the coalescence problem of multiple cracking.

2. Experimental procedures

2.1. Materials and methods

A BLT-S310 SLM additive manufacturing system was used to prepare the AlSi10Mg alloy blocks (110 × 55 × 120 mm^3). The AlSi10Mg powder was produced by the aerosol method having an average particle diameter between 15 and 45 μm and chemical composition is shown in Table 1.

The substrate material was 5A06 Al alloy and no preheating was performed. The processing parameters were explored over the following ranges: laser power between 360 and 400 W, scanning speed of 1200–1500 mm/s, hatch spacing of 0.13–0.16 mm, and a layer thickness of 50 μm achieved using a raster scan strategy with a 67° phase angle between successive layers. To eliminate the residual stress introduced by the SLM, the sample block was subsequently heated isothermally at 300 °C for 2 h and then cooled in a furnace. The AM build and heat treatment processes were carried out under an Ar atmosphere (O_2 content less than 100 ppm). Finally, the test-samples required for the various mechanical test experiments were cut parallel to the build direction of the block, as shown in Fig. 1. The surfaces of the test samples were polished along the axial direction of the specimen using progressively finer abrasive cloths to eliminate the influence of surface roughness.

Table 1
Chemical composition of the AlSi10Mg powder (wt. %).

Si	Mg	Fe	Cu	Mn	Trace elements	Al
9.0–11.0	0.4–0.6	≤ 2.0	≤ 0.6	≤ 0.35	0.25	Balance

2.2. Mechanical behaviors and fatigue resistance

Uniaxial tensile tests were performed using an MTS-810 Axial/Torsional testing machine on SLM-processed test-specimens having a gauge length of 25 mm and a diameter of 5 mm. The tensile load was applied under constant strain control. The gauge length of the extensometer was 25 mm, and the extension rate was 0.0002 s^{-1}. The load–displacement curve was recorded.

A QBG-50 high frequency testing machine was used to acquire the uniaxial tensile high cycle fatigue (HCF) curves of the SLM-processed AlSi10Mg specimens (gauge length of 15 mm and diameter of 5 mm) at five stress levels. Except for the lowest stress level, five specimens were tested at each stress level, giving a total of 20 samples. Tests at the lowest stress level were repeated for two specimens. A constant amplitude tension–tension loading with a stress ratio, R, of 0.1 and frequency, f, of 85 Hz was performed.

The width, W, and thickness, B, of the compact tension (C(T)) specimens were 40 mm and 5 mm, respectively. A notch 0.12 mm in width and 4 mm in length was prefabricated by electrical discharge machining. The fatigue crack growth (FCG) rate and threshold value were evaluated using an MTS ACUMEN3 testing machine. A sine waveform was used (f = 10 Hz, R = 0.1). According to the ISO 12108:2012 standard, the load shedding method was used for the threshold value.

The post-mortem uniaxial tensile HCF samples were observed using a TESCAN MIRA3 scanning electron microscope (SEM). Note that only some of the samples containing the fractured surfaces were analyzed to trace the critical defect.

2.3. X-ray micro tomography

Before the fatigue testing, laboratory X-ray CT scanning of the uniaxial tensile HCF specimens was performed using a Nikon XTH 225 micro-CT system to map the distribution and nature of the initial defects. The imaged height was 15 mm, and the voxel size was 9.0 μm, resulting in an equivalent diameter of 27 μm [26] for the minimum resolvable defect, and an exposure time of 1 s per projection. The tube voltage and current were 80 kV and 62 μA, respectively. Four projections were recorded at each acquisition angle using a step-scan mode. Within the range of 360°, projections were acquired every 0.25°. The projection images were then reconstructed using the filtered back-projection algorithm. After binarizing and thresholding, a three-dimensional (3D) rendering was reconstructed using AVIZO 9.1® 3D software. Afterward, the spatial distribution and morphological features of the defects near the fractured surfaces of some uniaxial tensile HCF samples were calculated.

2.4. In situ high cycle fatigue test

A fatigue test at 120 MPa with R = 0.1 on an HCF sample (specimen #23) cut parallel to the build direction was monitored by time-lapse CT using an *in situ* fatigue rig [27] placed on beamline (BL13W1) of the Shanghai Synchrotron Radiation Facility (SSRF) in Shanghai. The imaged height was 4 mm, and the pixel size was 3.25 μm. The photon energy was around 26 keV and an exposure time of 0.5 s per projection was used. One projection was recorded at each acquisition angle using a step-scan mode. Within the range of 180°, a projection was acquired every 0.25°, giving 720 projections for the volume reconstruction. The reconstruction and 3D rendering scheme for processing the projection images are the same as described in Section 2.3. Prior to testing, the specimen was scanned to determine the defect population. After 300,000 fatigue cycles (by which point large cracks are expected to have developed), the applied fatigue load was stopped and a static load (80% of the maximum stress applied under cyclic loading) applied. At this point, an X-ray CT scan of the specimen was carried out to confirm the geometry of the crack. Subsequently, the fatigue loading was resumed

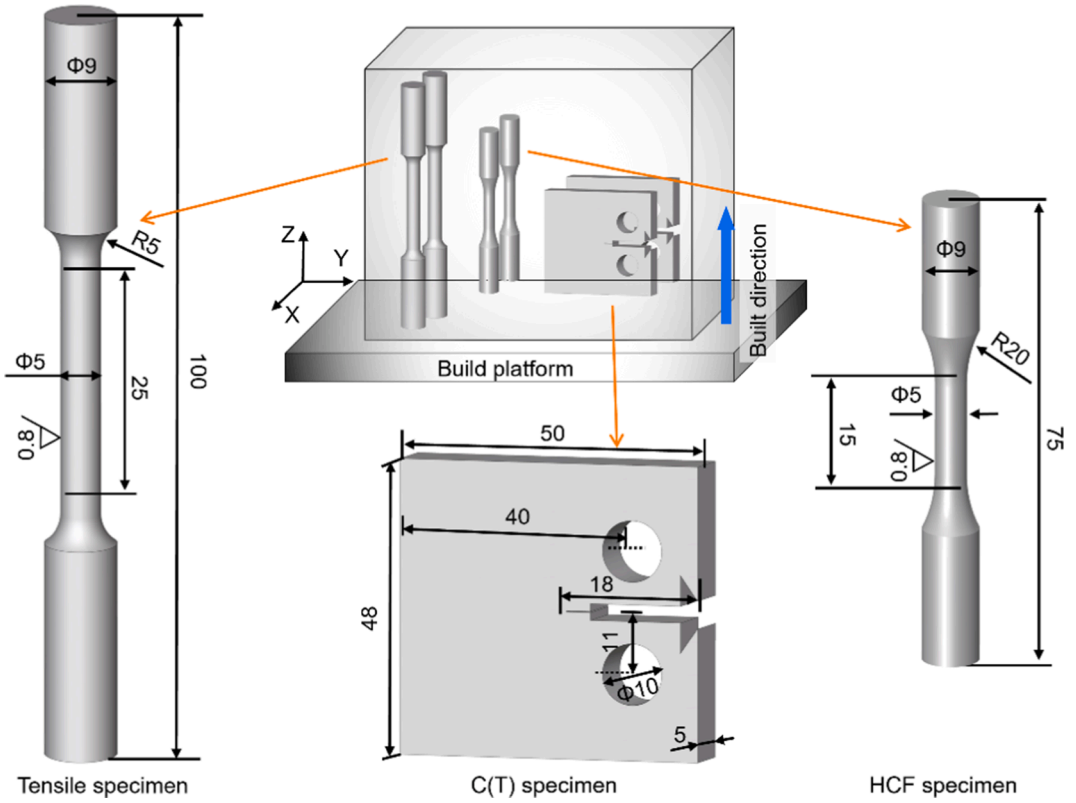

Fig. 1. Schematics showing the geometry of the test specimens and their orientation relative to the build direction (parallel to the Z-axis).

under identical loading conditions to resume crack extension until sample failure (after a further 34,587 cycles). After testing, post-mortem fractographic analysis was performed on the test-piece using a TESCAN MIRA3 SEM.

3. Results and analyses

3.1. Mechanical properties and fatigue lifetime

The mechanical properties of the SLM-processed AlSi10Mg alloys were measured by uniaxial tensile testing, as shown in Table 2.

In order to characterize the fatigue performance, the fatigue *S–N* response was plotted and fitted to Basquin's equation as illustrated in Fig. 2. The stress range here is the range between the maximum stress and the minimum stress.

3.2. Post-mortem fractographic analysis

Post-mortem analysis of the HCF fracture surfaces reveals regions of crack initiation, stable growth, and fast fracture. As demonstrated and discussed in more detail in Section 3.3, cracks tended to initiate from large LOF defects lying on, or near, the surface, which is similar to crack initiation from casting defects [28]. It is noteworthy that for the samples tested at the higher stress levels (samples #4, #9, #2, and #13), the failure mode involved the initiation of multiple cracks (see for example sample #4 in Fig. 3), which is consistent with the research of Uzan et al. [29]. These multiple cracks (marked with yellow boxes) merge during crack propagation, as evidenced by a ledge [20] (denoted by red arrows in Fig. 3) on the fracture surface, accelerating fatigue failure.

Table 2
Tensile properties of the SLM-processed AlSi10Mg alloys.

Specimen	Ultimate tensile strength σ_b/MPa	Yield strength $\sigma_{0.2}$/MPa	Elongation δ/%
#1	277	179	7.2
#2	273	181	6.3
#3	269	183	5.7
Average	273 ± 3.3	181 ± 1.6	6.4 ± 0.6

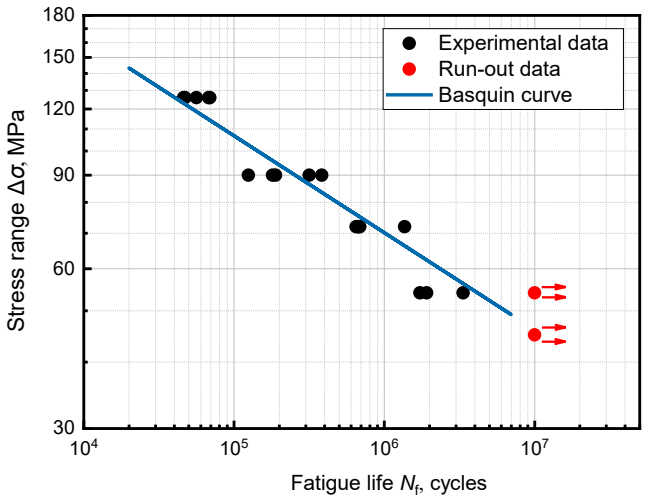

Fig. 2. High cycle fatigue *S–N* curve for the SLM-processed AlSi10Mg alloy.

3.3. Defect characterization

The spatial population and 3D morphology of the defects in the test pieces have been obtained by laboratory X-ray CT prior to the fatigue testing. From the 3D renderings (see Fig. 4(a) for an example) it is evident that there were a large number of defects, comprising small gas porosity defects and large LOF defects, essentially randomly distributed across the surface, near-surface, and interior regions of the specimen in

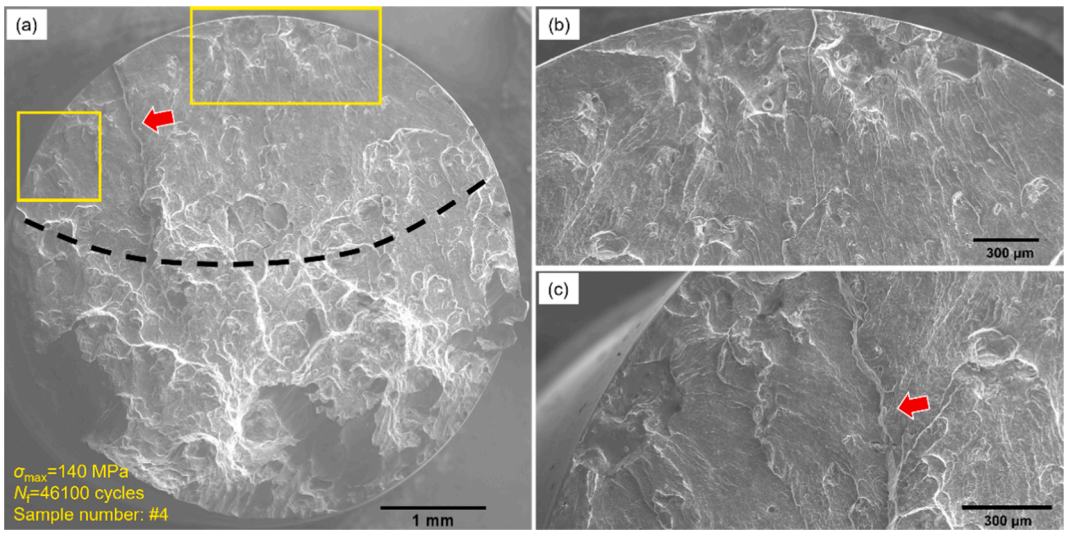

Fig. 3. SEM image of the fracture surface for HCF #4 specimen (a) with magnified regions of interest (b) and (c) showing crack initiation sites.

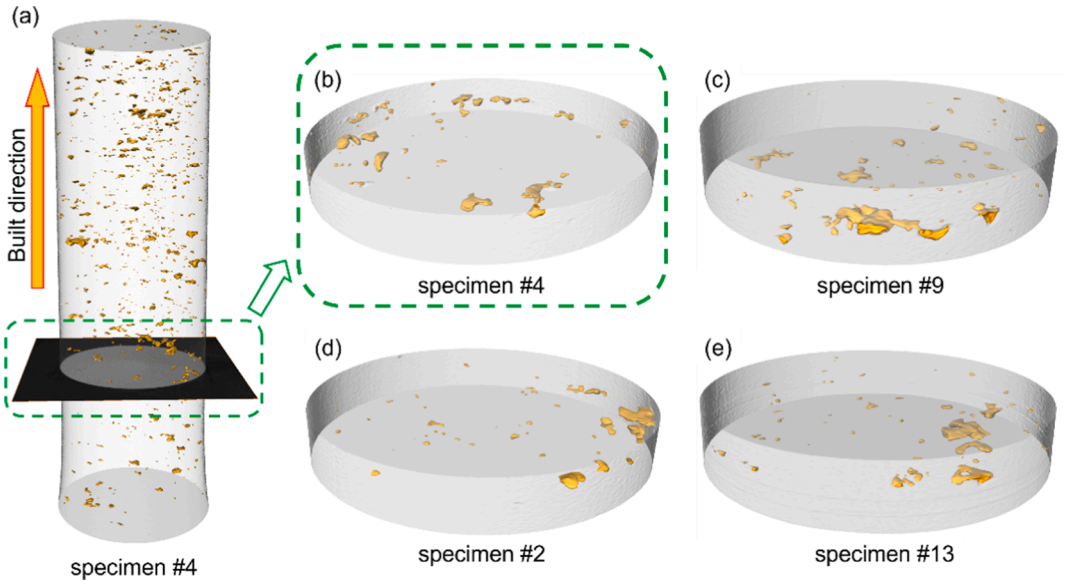

Fig. 4. (a) 3D rendering of the defect population in specimen #4 measured by X-ray CT, thick slice 3D renderings in the region of the final fracture for specimens b) #4c) #9, d) #2, and e) #13.

agreement with the previous work [30]. Moreover, the majority of the LOF defects exhibit a relatively flat 'pancake' shape perpendicular to the build (loading) direction, which would be expected to accelerate the fatigue crack initiation process for testing parallel to the build directions, as found previously [16]. To assess the original defect population in the vicinity of the fracture surfaces of #4, #9, #2, and #13 samples, thick slices corresponding to the location of the fracture planes were identified from the respective tomograms (Fig. 4(b-e)).

In Fig. 5 the defects in the vicinity of the fracture plane shown in Fig. 4(b-e) are projected onto the fracture surfaces for the specimens #4, #9, #2 and #13. These show a good correlation between the surface and near-surface initiation sites and the original defects. Furthermore, they suggest that some of the internal defects link up with the fatigue cracks during crack propagation and thereby influence the crack propagation process. Similar phenomena have also been reported in the study of Wu et al. [31]. Although the effect of defects on crack growth is still debated, namely whether they accelerate the crack growth, or blunt the crack tip suppressing crack growth, the link up of an internal defect with a propagating crack will instantly increase the area of the crack.

3.4. Crack propagation

To quantify the fatigue crack propagation process, Fig. 6(a) presents a 3D rendering of the initial defects in the region of the final fracture for specimen #23 (rendered in red) and the fatigue crack detected after 300,000 cycles (rendered in yellow) from the *in situ* time-lapse CT scan, described in Section 2.4. It can be seen that crack initiates from the surface and near-surface defects in agreement with the observations of the aforementioned *ex situ* experiments. The sections and renderings in Fig. 6 clearly show a relatively flat propagation path of the fatigue crack and a regular elliptical crack front. In addition, the crack in the CT scan stage propagated to fracture after 34,587 cycles of loading, which will be further discussed in Section 4.1 to verify the work in this paper.

3.5. Crack growth behavior

The measured fatigue crack growth rate, da/dN, versus SIF range, ΔK, curve of the SLM-processed AlSi10Mg alloy C(T) samples are plotted in Fig. 7. It should be borne in mind that the fatigue crack growth data

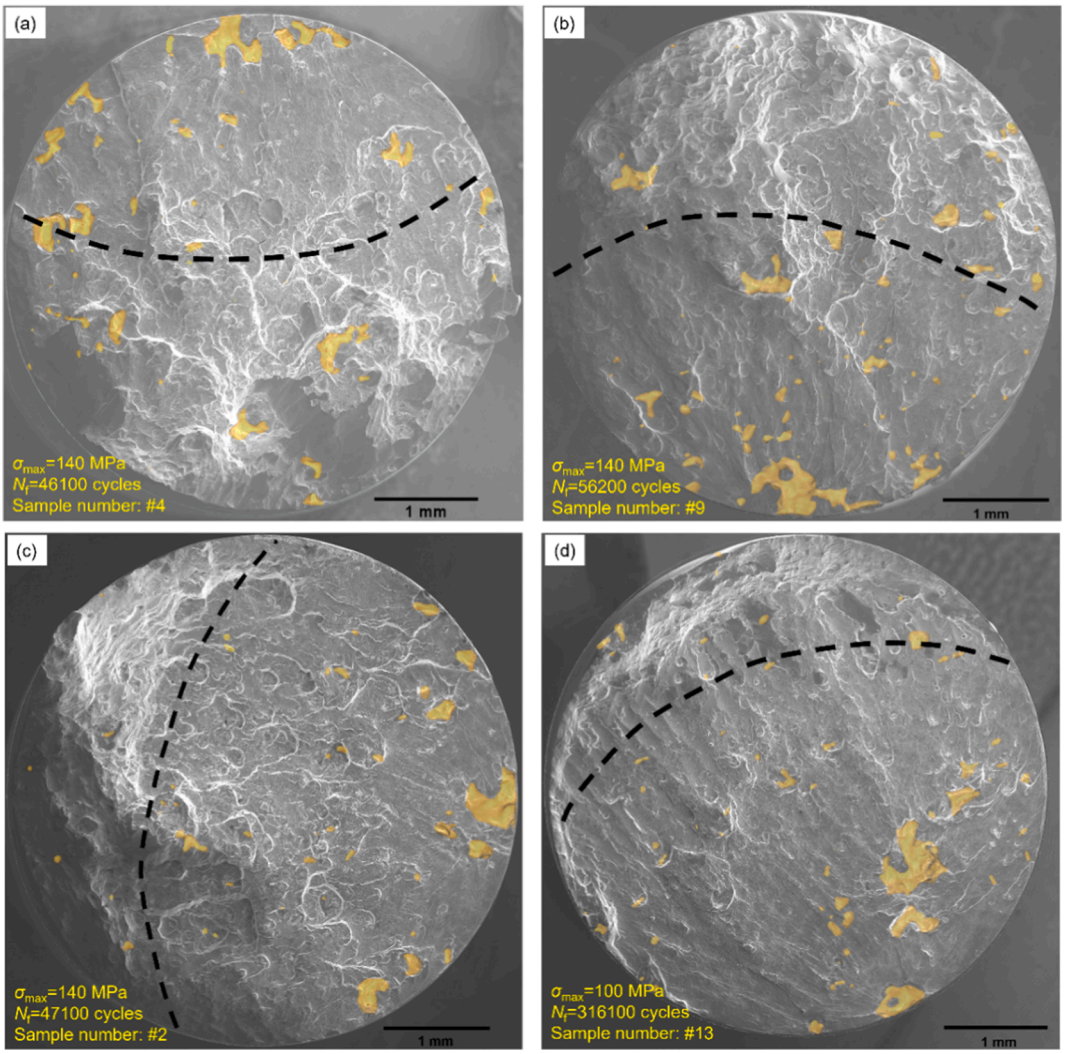

Fig. 5. Superposition of the projections of defects in the 3D thick slice X-ray CT volume renderings (yellow) onto the fracture surfaces for specimens a) #4, b) #9, c) #2, and d) #13. (For interpretation of the references to colour in this figure legend, the reader is referred to the web version of this article.)

were performed on AM alloy material produced in the same manner and thus containing defects similar to those recorded by X-ray CT for the fatigue samples. As a result, the da/dN–ΔK curves shown in Fig. 7 are not strictly indicative of the crack propagation resistance of defect free material. In principle it would be preferable to determine the FCG law for defect free material – but it is not practical to obtain damage free material having the same microstructure as the AM samples. Therefore, the effect of this error is not considered in this paper, as this issue is beyond the scope of this study.

From the curve, we observe that the threshold region exhibits a relatively broad scatter, which is probably due to multiple defects affecting the very short crack growth phase. In general, the entire cracking region can be described well using the simplified NASGRO equation [14,32] considering the crack closure effect:

$$\frac{da}{dN} = C\left[\left(\frac{1-f}{1-R}\right)\Delta K\right]^{n}\left[1-\frac{\Delta K_{th,l}}{\Delta K}\right]^{P}, \tag{1}$$

where C, n, and P are material constants, and $\Delta K_{th,l}$ is the SIF range of the long crack growth threshold (approximately 1.21 MPa·m$^{1/2}$ taken at da/dN = 1x10^{-7} mm/cycle by linearly fitting the data points between 1x10^{-6} – 1x10^{-7} mm/cycle). f is the crack opening function as follows:

$$f = \frac{K_{op}}{K_{max}} = \begin{cases} max\left(R, A_0 + A_1 \cdot R + A_2 \cdot R^2 + A_3 \cdot R^3\right) & R \geqslant 0 \\ A_0 + A_1 \cdot R & -2 \leqslant R < 0 \end{cases}, \tag{2}$$

$$\begin{aligned} A_0 &= \left(0.825 - 0.34\cdot\alpha + 0.05\cdot\alpha^2\right)\cdot\left[cos\left(\frac{\pi\sigma_{max}}{2\sigma_0}\right)\right]^{1/\alpha}, A_1 \\ &= (0.415 - 0.071\cdot\alpha)\cdot\left(\frac{\sigma_{max}}{\sigma_0}\right), A_2 = 1 - A_0 - A_1 - A_3, A_3 \\ &= 2A_0 + A_1 - 1, \end{aligned} \tag{3}$$

where K_{op} is the opening SIF, K_{max} is the maximum SIF, α is the constraint factor, σ_{max} is maximum stress, and σ_0 is the flow stress. Considering the experiment was in a plane strain state, α for the Al alloy could range from 1.7 to 2.0 [33]; α was taken as 1.85 here. In NASGRO, $\sigma_{max}/\sigma_0 = 0.3$ is usually adopted for the parameter fitting for most engineering materials and was used here; thus, $f = 0.36$. Inserting f into Eq. (1), the logarithm of the expression becomes

$$\log\frac{da}{dN} = \log C + n\cdot\log[0.7099\Delta K] + P\cdot\log\left[1-\frac{\Delta K_{th,l}}{\Delta K}\right]. \tag{4}$$

The NASGRO curve is shown in Fig. 7 with the values of log$C$, n, and P taken to be − 5.76, 2.51, and 0.77, respectively, which are obtained by best fit to the data in Fig. 7.

4. Fatigue crack propagation life prediction

Under high stress levels, the fracture surface often shows evidence of

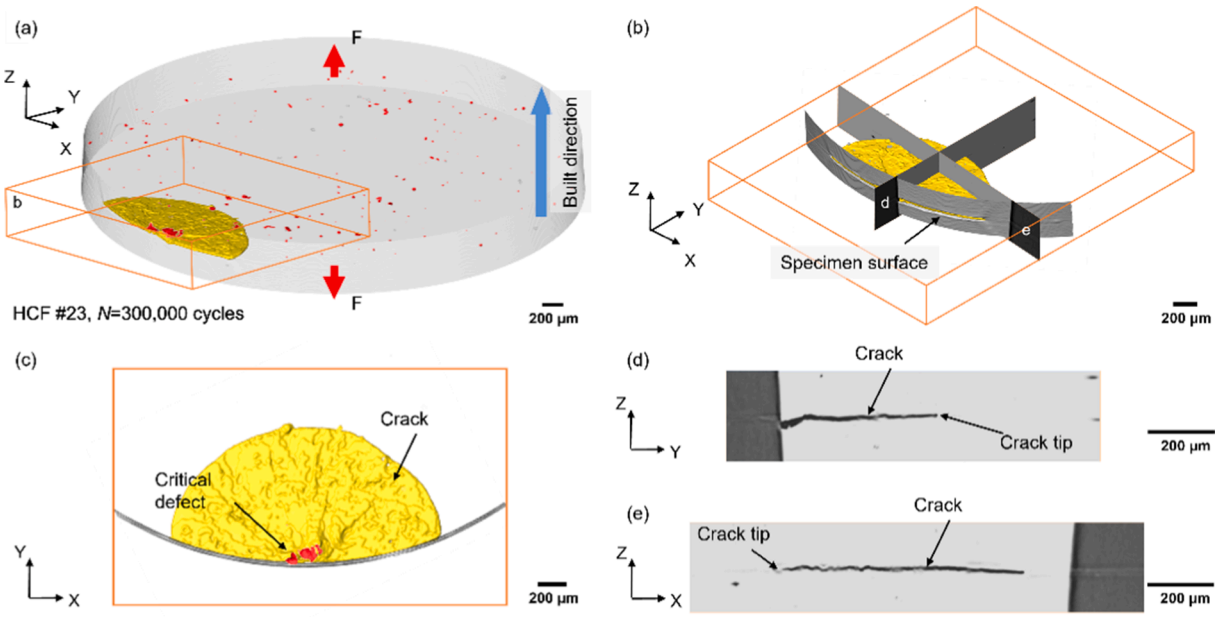

Fig. 6. (a) 3D rendering of initial defects (rendered red) and crack detected after 300,000 cycles (rendered yellow) (b) a magnified regions of interest containing the crack; (c) plan view of the rendered crack; (d) and (e) virtual cross sections of the crack at locations defined in (b). (For interpretation of the references to colour in this figure legend, the reader is referred to the web version of this article.)

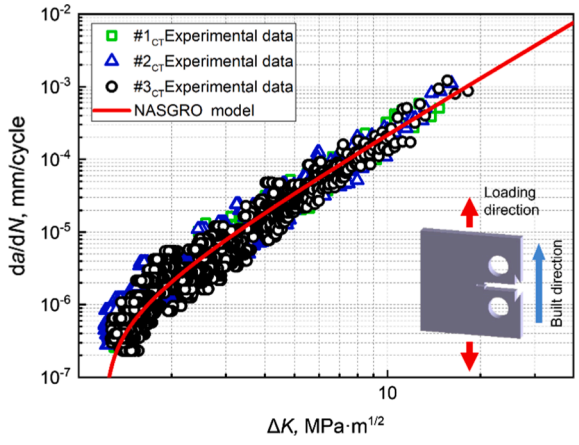

Fig. 7. FCG test data for samples $\#1_{CT}$, $\#2_{CT}$ and $\#3_{CT}$ alongside the NASGRO curve of SLM-processed AlSi10Mg alloys ($R = 0.1$).

initiation from multiple defects, which is consistent with the previous literature [29,34]. When multiple defects contribute to fatigue fracture, an individual fatigue crack or critical defect-based growth model naturally leads to a non-conservative assessment [21,35]. To this end, the current work attempts to establish a novel FCG model that considers multiple defects for a more accurate prediction of the fatigue life.

4.1. Critical defect-based crack growth

It is generally argued that an individual defect is responsible for increasing the local stress, which eventually initiates a short fatigue crack under external loading [36]. Crack growth occurs when it can penetrate the material barriers ahead of the critical defect. For the SLM-processed metallic alloys, the randomly distributed defects determine the fatigue resistance. As a crack initiates and grows from a defect, the stress concentration arising from that defect fades away. After a short length of crack extension (at the scale of a short crack), the defect can be regarded as a part of the crack. Considering the scale of short cracks is generally small compared to the defect size, we define the initial crack to be the circumscribed semi-ellipse of the critical defect to simplify the calculation so as to focus on the long crack growth. It should be noted that the circumscribed ellipse needs to satisfy the following conditions: the center is located on the surface of the sample and the major axis lies at a tangent to the surface by definition the minor axis is shorter than the major axis.

As described in Section 3.2, the fatigue test samples in this paper all failed from surface or near-surface defects. Here we define internal defects as lying at a distance, d, from the surface greater than a defect dimension ($\sqrt{area} < d$) and these are not considered here. Instead, we consider surface and near-surface defects in Fig. 8. It should be noted that neighboring defects are treated separately according to Fig. 8(a) and (b) if $d_2 + d_3 < d_1$, while they are considered as a single defect if $d_2 + d_3 > d_1$ as shown in Fig. 8(c) and (d). In addition, except for the largest initial crack, the remaining initial cracks and initial defects are only considered in the smFCG model established in Section 4.2. The single crack model described in this section only considers the largest initial crack after the critical defects are regularized. Based on this approach, the critical defects on the fracture surface of all fatigue test samples were measured, and the results (semi major axis (a) and semi minor axis (b)) are listed in Table 3 and Table 4.

For the special case shown in Fig. 9(a), the surface semi-elliptic crack front can be described by the parametric equation of a standard elliptic:

$$\begin{cases} x = a\cos(\theta) \\ y = b\sin(\theta) \end{cases} \quad 0 \leqslant \theta \leqslant \pi, \tag{5}$$

where a and b are the semi major and semi minor axes of the ellipse, respectively. For the general case where the angle between the major axis and the x-axis is α and the center is located at (x_0, y_0), the surface semi-elliptic crack can be described by the standard elliptic equation through the coordinate transformation:

$$\begin{cases} x' = x\cos(\alpha) - y\sin(\alpha) + x_0 \\ y' = x\sin(\alpha) + y\cos(\alpha) + y_0 \end{cases} \quad 0 \leqslant \alpha \leqslant 2\pi, \tag{6}$$

Based on Eq. (5) and (6), a semi-elliptical surface crack at any position can be described by a simple standard form, which greatly simplifies the numerical calculation process. With the geometrical

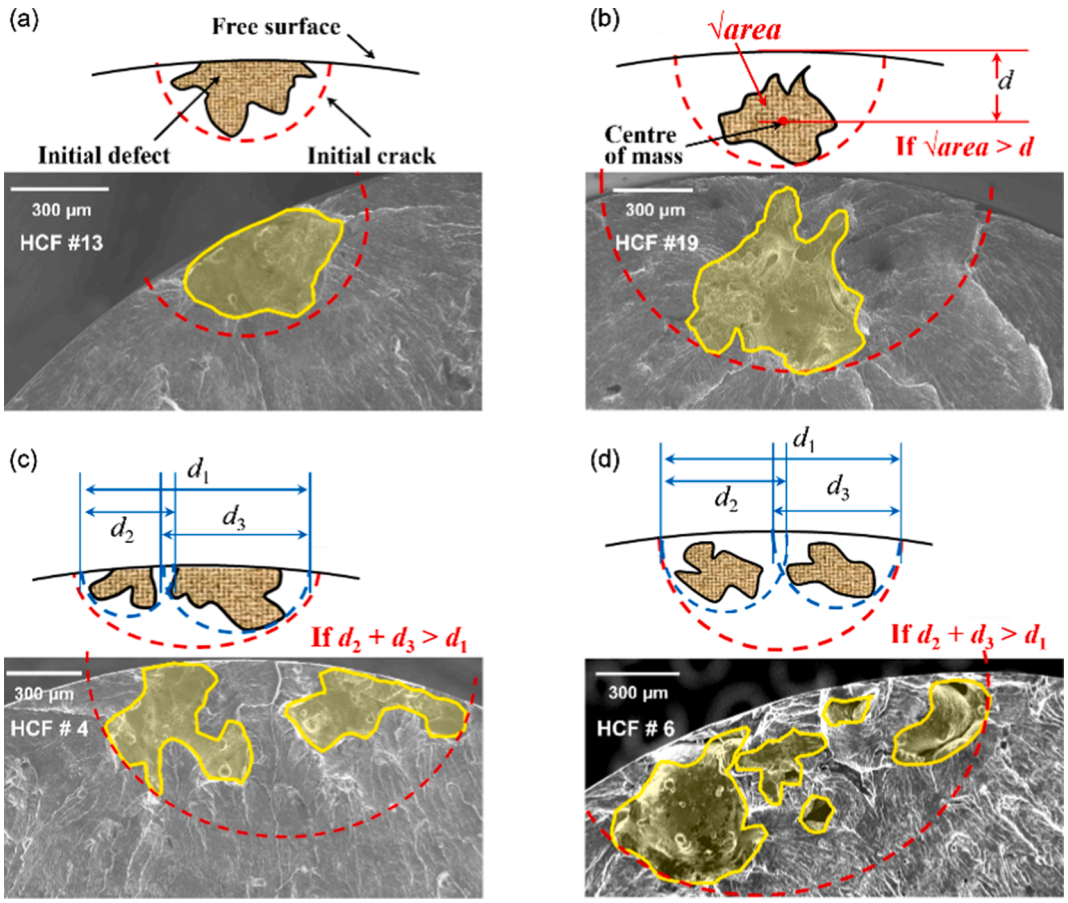

Fig. 8. Regularization criteria for critical defects in fatigue modeling: (a) a surface defect, (b) a near-surface defect, (c) multiple surface defects, and (d) multiple near-surface defects.

Table 3
Calculated fatigue crack growth lifetime using the single crack model compared to experiment.

Sample number	σ_{max}/MPa	Measured fatigue life/cycles	Semi major axis (a)/mm	Semi minor axis (b)/mm	Predicted propagation life/cycles	% of measured life
#04	140	46,100	0.780	0.700	25,200	55%
#09	140	56,200	0.675	0.590	31,600	56%
#02	140	47,100	0.650	0.620	31,700	67%
#22	140	69,100	0.525	0.515	41,300	60%
#07	140	67,900	0.550	0.505	40,300	59%
#12	100	384,100	0.380	0.375	164,100	43%
#13	100	316,100	0.360	0.340	179,300	57%
#19	100	180,200	0.730	0.715	67,300	37%
#06	100	124,800	0.780	0.680	65,500	52%
#21	100	188,700	0.540	0.530	104,600	55%
#20	80	687,800	0.350	0.340	402,400	59%
#01	80	674,700	0.390	0.335	368,900	55%
#18	80	648,700	0.380	0.340	373,700	58%
#11	80	1,364,800	0.320	0.300	481,600	35%
#05	80	669,800	0.500	0.450	247,400	37%
#03	60	1,917,300	0.460	0.440	898,500	47%
#14	60	3,350,000	0.425	0.410	1,213,750	36%
#17	60	1,726,300	0.515	0.510	658,350	38%
#10	60	Run-out	—	—	—	—
#15	60	Run-out	—	—	—	—
#16	50	Run-out	—	—	—	—
#08	50	Run-out	—	—	—	—

dimension parameters defined in Fig. 9(a), the SIF, K_I, of the semi-elliptical surface cracks can be expressed in the following form:

$$K_I = Y\sigma\sqrt{\pi b}, \tag{7}$$

where Y is the geometry correction factor, and σ is the uniform axial stress. Considering the symmetry relationship, Shin et al. [37] calculated Y for seven typical points along the half-crack front ($x/h = 0.000$, 0.167, 0.333, 0.500, 0.667, 0.833, and 1.000) under different crack depths (b/D) and aspect ratios (b/a) using the FE method. Further, they proposed closed-form equations of Y by using multi-parameter fitting technique as follows:

Table 4
Calculated fatigue crack growth lifetime using the novel smFCG model.

Sample number	σ_{max}/MPa	Measured fatigue life/cycles	Semi major axis (a)/mm	Semi minor axis (b)/mm	Predicted propagation Life/cycles	% of measured life
#04	140	46,100	0.780	0.700	23,100	50%
			0.310	0.300		
			0.295	0.285		
#09	140	56,200	0.675	0.590	25,600	46%
			0.295	0.290		
#02	140	47,100	0.650	0.620	27,400	58%
			0.265	0.250		
			0.240	0.235		
#13	100	316,100	0.360	0.340	148,600	47%
			0.225	0.215		

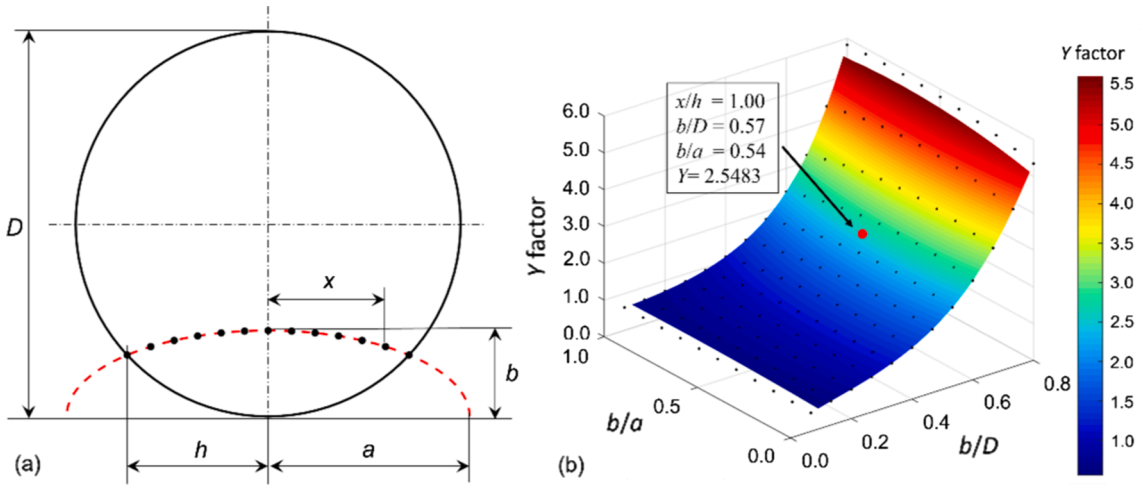

Fig. 9. (a) Schematic diagram of the geometrical parameters defining the surface semi-ellipse crack along with the seven representative locations at which response surfaces have been constructed, (b) the Y response surface for $x/h = 1$.

$$Y = Y\left(\frac{b}{a}, \frac{b}{D}, \frac{x}{h}\right) = \sum_{i=0}^{2}\sum_{j=0}^{7}\sum_{k=0}^{2} M_{ijk}\left(\frac{b}{a}\right)^{i}\left(\frac{b}{D}\right)^{j}\left(\frac{x}{h}\right)^{k}, \text{ for tension,} \quad (8)$$

where M_{ijk} is the coefficients that depend on the values of i, j, and k. In this work, we prefer to use a simplified version of the closed-form equation. Based on the research of Shin et al. [37], seven Y response surfaces [38] were constructed for seven representative points along the half-crack front to obtain the Y of each typical point as a function of b/D and b/a. An example plot of Y response surface is shown in Fig. 9(b) where the black dots are the results calculated according to Shin et al. [37] and the red dot is an arbitrary point on the surface.

The single crack model described in this section is shown schematically in Fig. 10(a), which includes the following four steps:

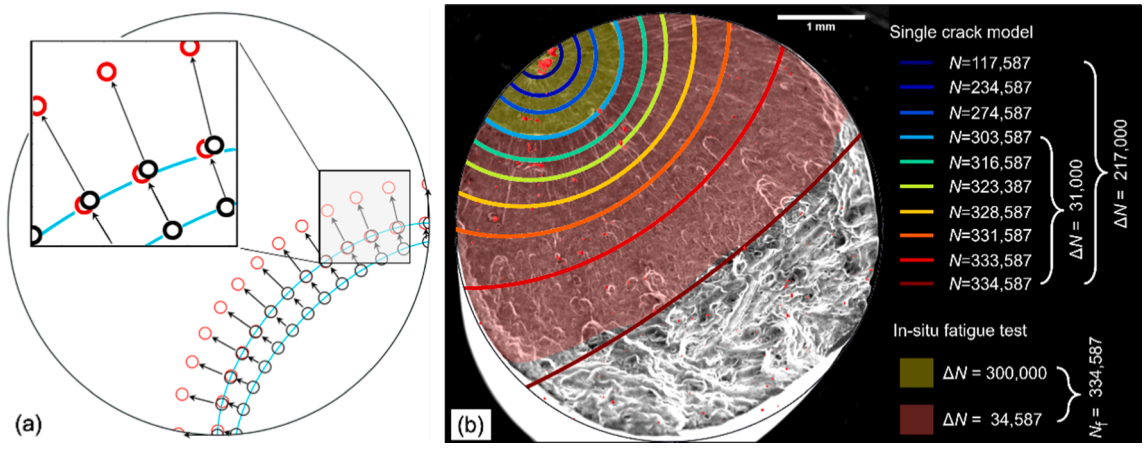

Fig. 10. (a) Schematic diagram of the single crack model, and (b) superposition of the modelled crack growth sequence onto the fracture surface for specimen #23, which failed after 34,587 cycles from the moment of interrupted *in situ* imaging. The extent of the fatigue crack at 300,000 (from X-ray CT) and at final fracture are shown by yellow and red tints respectively. (For interpretation of the references to colour in this figure legend, the reader is referred to the web version of this article.)

- Step 1. The representative growth points ($x/h = 0.000$, 0.167, 0.333, 0.500, 0.667, 0.833, and 1.000, as shown by the black spots) are identified on the crack front (blue curve).
- Step 2. ΔK is determined for each representative growth point from the respective Y response surface.
- Step 3. The representative growth points are moved perpendicular to the semi-ellipse crack front according to the NASGRO law.
- Step 4. The resulting representative growth points (red spots) are fitted to a semi-ellipse (blue curve) representing the new crack front.

This process was repeated iteratively until the $K_{I,max}$ for the crack front reached the critical value ($K_{IC} = 25$ MPa·m$^{1/2}$, according to the da/dN–ΔK curve and literature reports [1,39]), representing the crack growth life N of the sample. Since the total crack growth for an increment of 100 loading cycles is very small, the distribution of ΔK along the crack front was considered to be static over 100 cycles thereby reducing the number of iterations in the calculation by a factor of 100.

For the *in situ* HCF test for specimen #23, described in Section 2.4, the crack initiated which from a critical near-surface defect was detected after 300,000 cycles of loading as illustrated in Fig. 10(b) by the yellow shading. Then, the crack in the CT scan stage propagated to fracture after 34,587 cycles of additional loading, as shown by the red shading in Fig. 10(b). In order to evaluate the model, superposition of the modelled crack growth sequence (the calculation result based on the single crack model, as shown in the colored arcs) onto the fracture surface for specimen #23 is shown in Fig. 10(b). Since we do not know the crack initiation life the fatigue crack propagation sequence is derived backwards in time by defining the front at fast fracture as the 334,587th cycle. In the red shaded area, although this model gives a faster crack growth rate at the later stage of crack growth, this has little effect on the prediction of the crack growth life (the calculation error is about 10%), and the crack front morphology is well predicted. This suggests that the model is appropriate to describe our *ex situ* tests. In the yellow shaded area (corresponding to the crack front at 300,000 cycles), the smallest colored arc is the initial crack defined by the defect regularization method used in the model. This points back to propagation after 117,587 cycles of loading, i.e., the crack propagation life predicted by the model accounts for approximately 65% of the total fatigue lifetime. The fatigue life for this sample is a little longer than one might expect in view of the results at $\sigma_{max} = 140$ and 100 in Table 3 and this may be due to the different experimental conditions between the *in situ* and *ex situ* experiments. Therefore, sample #23 was not considered in the discussion of the contribution of crack initiation life to the total fatigue life. Anyways the results suggest that the crack growth behavior of the single crack initiation cases are well represented by this model. Based on the single crack model, the fatigue lives of the samples fatigue tested in this paper are compared with the model predictions in Table 3.

In common with the results in Fig. 10(b), Tammas Williams et al. [15] also found that for AM-processed Ti alloy the initiation stage can make up a large fraction of the life. It is also clear from Table 3 that the propagation life is predicted on the basis of the single crack model to become a larger fraction of the total life as the applied stress is increased. It is noteworthy that the predicted propagation life of sample #19 was lower, which may be due to the regularization criteria being too conservative for defects that deviate from the semi-elliptic assumption, as shown in Fig. 8(b). However, the results suggest that for most cases, the current regularization method is still applicable.

4.2. Multiple defect-induced crack growth

In the previous section, the fatigue crack growth life of all the HCF samples was predicted based on the single crack model. But when multiple defects are associated with initiation the critical defect-based growth model naturally leads to a non-conservative assessment. In addition, the large internal defects close to the initiation sites may have a significant effect on crack propagation. The failure mode of welded structures containing multiple fatigue cracks has been extensively studied but AM-processed metals have received little attention. Based on the defect characterization, here we seek to establish a crack propagation life evaluation method that considers multiple fatigue cracks and initial defects. Note that in the actual multiple crack propagation problem, the fracture surfaces that merge to form the final crack are not all located on a single plane. This is neglected here where we consider all the fatigue cracks participating in the final fractured surface to be located on the same plane, and subsequent discussions are conducted under this premise. In effect this flattens the defects in the thick slices shown in Fig. 4 into a single plane.

The evolution of multiple cracks can be divided into three stages: pre-coalescence, coalescence, and post-coalescence [40]. Although the interaction of the crack fronts enlarges the SIF range and accelerates the growth of adjacent tips, this effect is minimal until two cracks come into contact. Before the cracks coalesce, they are considered to expand according to a semi-elliptical geometry, with only the radius increasing. For two surface semi-elliptical long cracks such as those considered in this paper, the duration of the coalescence process is very short. In the final stage, as the ΔK at the crack front gradually returns to the normal level, the corresponding growth rate also tends to be normal. Therefore, the criterion for crack coalescence given in section XI of the early ASME code is considered to be conservative [40,41], and the subsequent no-interaction and immediate transition (NIIT) method is widely used [19,21,34,40]. The NIIT method means that the interaction of two adjacent cracks before merging is ignored, and when the two cracks contact, they instantly transform into one crack (the length is the sum of the two cracks, the depth is the maximum depth of the two cracks, and the crack front remains semi-elliptical in all cases). The current study works with the coalescence problem of multiple cracks based on the NIIT method.

The basic calculation process of the smFCG model is the same as that of the single crack model, but further criteria have been added to consider the effects of multiple cracks and internal defects on crack propagation at the same time. The calculation process for the smFCG model is shown in Fig. 11 and includes the following five steps:

- Step 1. Determining the form of the initial cracks (each represented by a semi-ellipse based on Fig. 8) and internal defects (each represented by a circle having the same projected area) from the X-ray CT imaging prior to fatigue testing and post-mortem analysis.
- Step 2. Propagating each crack independently based on a single crack model.
- Step 3. Determining whether the fast fracture conditions are met ($K_{I,max} = K_{IC} = 25$ MPa·m$^{1/2}$).
- Step 4. Determining whether the crack coalescence conditions are met. When two cracks (#i and #j) contact, $a_{new} = a_i + a_j$, $b_{new} = \max\{b_i, b_j\}$, and the center is located at the midpoint of the surface intersection line. When a crack is in contact with any defect, the coalescence process is an equal-area transformation (uniformly propagating the crack front) with the center remaining unchanged.
- Step 5. Updating the crack front.

Considering the complexity and universality of the above-mentioned multiple crack propagation process simulation, the samples #2 and #13 were considered to demonstrate the application of the novel smFCG model. As shown in Fig. 12(a), with increasing number of loading cycles, the aspect ratio of cracks #2 and #3 increased, while the aspect ratio of crack #1 decreased. After 16,200 fatigue cycles, cracks #2 and #3 came into contact with each other and merged immediately, forming a new crack with a sudden decrease in aspect ratio. After 23,100 cycles, the main crack, ultimately formed by the secondary merger, continued to expand. In the main crack propagation stage, the aspect ratio first increased and then decreased to about 0.6, which is consistent with the results reported in the literature [41–43]. As shown by sample #13 (Fig. 12(b)), the merging of large internal defects with the main crack

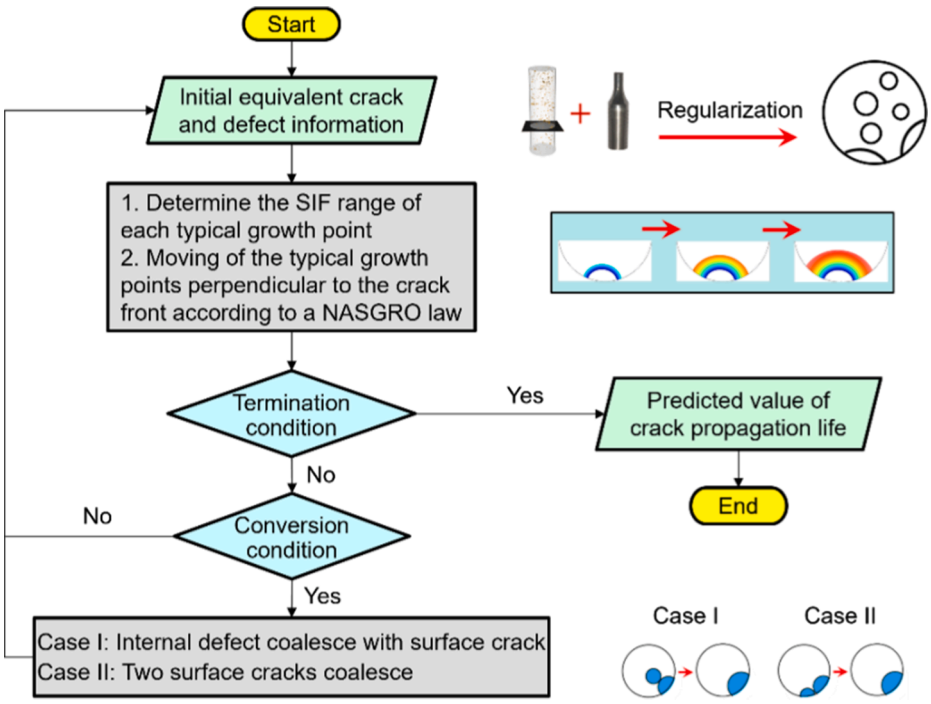

Fig. 11. Fatigue crack growth prediction flowchart using the smFCG method for the SLM-processed alloys.

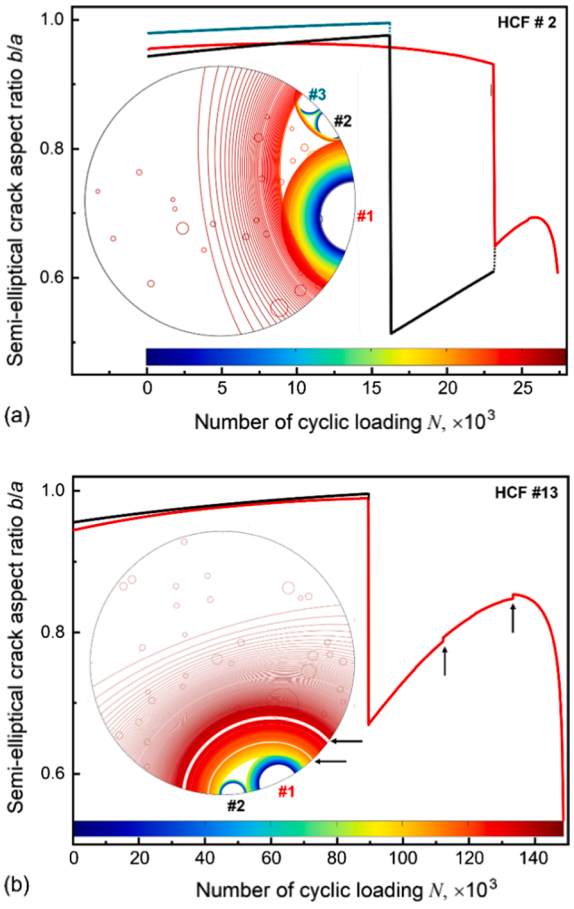

Fig. 12. Schematics of the multiple crack propagation simulations for HCF sample #2 (a) and sample #13 (b) based on the original defect populations determined a priori by X-ray CT.

led to a sudden change in the area, which, in turn, led to the white bands in the figure. At the same time, the crack aspect ratio has changed abruptly, as shown by the black arrow in Fig. 12(b).

The crack growth life assessment of samples #4, #9, #2, and #13 obtained on the basis of the newly proposed smFCG model, is shown in Table 4. Combining the fracture morphologies from Section 3.3 and the calculation results of the single crack model in Section 4.1, we can see that the smFCG model predicts a crack propagation life which is more conservative compared to the single crack growth model.

Comparing the results for specimens #2, #4, #9, and #13 between Table 3 and Table 4 it is clear that the propagation lives fall by around 5–10% of the total life on taking into account the multiple cracks. Further it would suggest that the crack initiation life accounts for approximately 40 to 65% of the total fatigue lifetime. Based on a quasi-in-situ fatigue experiment, Biswal et al. [44] observed that the crack initiation life induced by pore defects comprised approximately 70 to 80% of the total life. This result is higher than that inferred from the smFCG results or our own *in situ* test. This may be explained by the fact that the critical defects described in the current study were large LOF defects with relatively flat shapes perpendicular to the loading direction. Their sharp edges are more conducive to fatigue cracking than the smooth surface of pore defects, which significantly shortened the crack initiation lifetime.

5. Discussion

5.1. Multiple crack coupling

Although the predicted results were satisfactory based on the NIIT method, the effect of the coupling of cracks on the fatigue crack propagation life has been neglected. Here, we attempt to explore the extent of the interaction between neighboring cracks as a function of their separation so as to identify when this is an important consideration.

In order to evaluate the distance over which neighboring cracks couple, a series of cuboids were considered, each containing two semi-circular surface cracks separated by a certain distance, and the SIFs of the tip were solved via an elastic FE simulation. The radius $\dot{R}$ of each semi-circular surface crack is 0.25 mm, and the separation between

them, d_0, is $0.2\acute{R}$, $0.5\acute{R}$, $1.0\acute{R}$, $2.0\acute{R}$, $3.0\acute{R}$, $4.0\acute{R}$, respectively. A tube with collapsed quadratic brick elements at the center line was used to mesh the crack tip. The mid-side nodes were moved to the quarter of the sides adjoining the collapsed edges to create the $1/\sqrt{r}$ singularity of the strain field at the crack tip. To balance the competing demands between calculation accuracy and modeling accuracy, fine quadratic brick elements were used only for the crack surface, and quadratic tetrahedral elements filled the outside. The minimum element size (collapsed quadratic brick elements) was 0.0025 mm, and a stress of 80 MPa was applied. Finally, the SIFs were solved by the interaction integral method, which can be expressed as follow:

$$M = \oint_C \left(Wn_i x_i - T_k u_{k,i} x_i\right) \mathrm{d}s \tag{9}$$

where C is an integral path around the crack, W is the strain energy density, n_i is the outward normal unit vector of curve C, T_k is the traction force acting on the outside of the path, $u_{k,i}$ is the reference displacement, and x_i is the reference coordinate. The above modeling and calculation processes are shown in Fig. 13.

Fig. 14 shows a comparison of the SIF results from the coupled multiple crack simulations. A drop in K_I at the surface intersection points is evident and occurs because the power of the singularity there is no longer $-1/2$, which makes it difficult to obtain a correct estimate of K_I in the region close to the free surface [45]. Since the aim is only a qualitative analysis of the coupling effect between the cracks, the error in the K_I at the surface intersection points has not been corrected. Overall, the K_I near the surface is greater than that at the inner point, which is consistent with the K_I distribution for semi-elliptical surface cracks. It can be seen that the effect of coupling on K_I is negligible when the two cracks are far apart ($d_0 > 1.0\acute{R}$). Not surprisingly, as the separation distance decreases ($d_0 = 0.5\,\acute{R}$), the K_I of the adjacent parts of the two cracks increases, indicating that the coupling effect between the two cracks gradually increases. Further, when the two cracks are relatively close ($d_0 = 0.2\acute{R}$), a significant increase (about 20%) in the K_I is observed. By this point, the two cracks have a tendency to rapidly expand and merge. Note that in the non-adjacent parts of the two cracks, no significant increase in K_I could be observed in any case. In summary, when the two cracks are relatively close, the K_I increased significantly at the minimum interval, which provides a reference for improving the smFCG model.

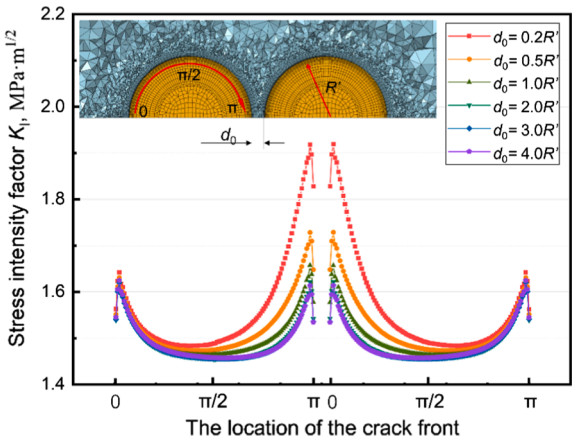

Fig. 14. Comparison of the dependence of K_I results across the crack fronts as a function of crack separation.

In addition, the FCG experiments were performed on C(T) specimens (specimens with through-crack and limited thickness), and the da/dN–ΔK curve was fitted from the test data as the basis for evaluating the crack growth life. However, it is known that the constrained state of the crack tip will transition from plane stress conditions at the surface to plane strain in the interior. Therefore, the da/dN–ΔK curve obtained from the test cannot describe the growth characteristics of the semi-elliptical crack front. This work has overlooked this effect, and a certain degree of error is generated. In this regard, Guo et al. [46] proposed a correction to the semi-elliptical crack front using a 3D modified strip-yield model [47,48] and the equivalent thickness B_{eq} [48,49] as shown in Eq. (10)–(13).

$$\frac{K_{op}}{K_{max}} = 1 - \sqrt[3]{\frac{\left(1-R^2\right)^2\left(1+10.34R^2\right)}{\left(1+1.67R^{1.61}+\frac{1}{0.15\pi^2\alpha_g}\right)^{4.6}}} \tag{10}$$

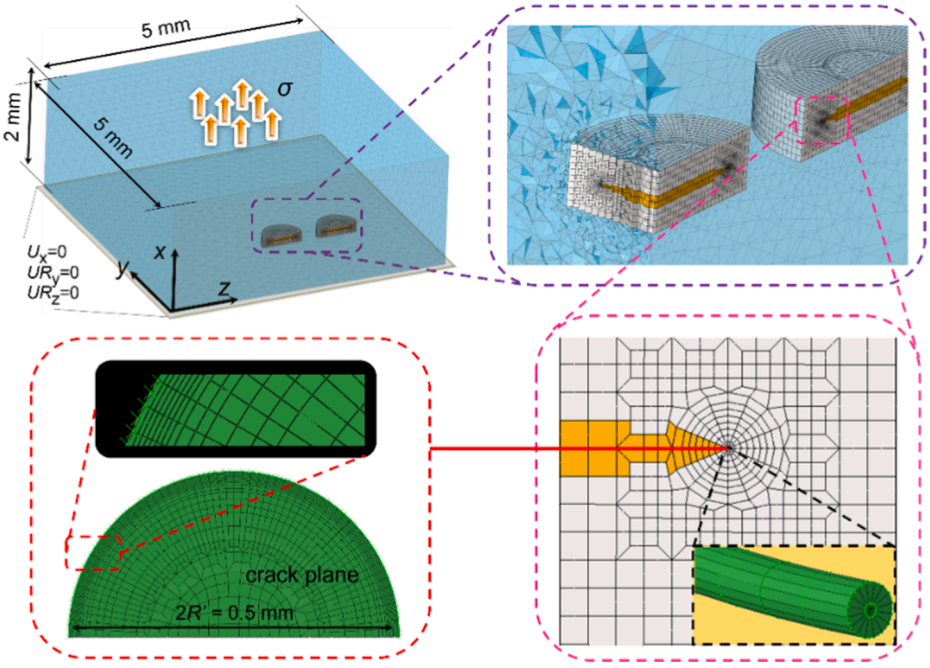

Fig. 13. Schematic diagram of the fatigue crack model and mesh.

$$\alpha_g = \frac{1 + 0.2088\left(r_{p0}/B_{eq}\right)^{0.5} + 1.5046\left(r_{p0}/B_{eq}\right)}{1 - 2\nu + 0.2088\left(r_{p0}/B_{eq}\right)^{0.5} + 1.5046\left(r_{p0}/B_{eq}\right)} \quad (11)$$

$$r_{p0} = \frac{\pi}{8}\left(\frac{K_{max}}{\sigma_0}\right)^2 \quad (12)$$

$$B_{eq} = a\left[1 - \left(\frac{\pi/2 - \varphi}{\pi/2}\right)^{6t}\right],\ 0 < \varphi < \pi/2 \quad (13)$$

where α_g is a combined constraint factor considering 3D stress state of crack, r_{p0} is crack-tip plastic zone size under plane stress, ν is Poisson's ratio, φ is the directional angle of ellipse, and t is the shape factor of ellipse determined as the ratio of minor axis to major axis. According to Eq. (10)–(13), the effective SIF range, ΔK_{eff}, at a certain location of the crack front can be obtained. Then, based on the unique da/dN–ΔK_{eff} curve of the material, the above issue could be resolved. Pang et al. [41] also adopted ΔK_{eff} as the crack growth driving force. Based on these methods, the difference in the constrained state of the crack front could be considered, which might facilitate the simulation of the crack growth process.

5.2. Whole fatigue life assessment

The current study has only evaluated the fatigue crack propagation life, and in the future, crack initiation should be included. Although the specimens under low loading level experienced an elastic deformation, the internal defects were subjected to a partial plastic yielding because of the higher stress concentration. This suggests a local stress–strain method [50] could be an effective approach. Moreover, *in situ* fatigue tests provide advanced insight into the evolution of fatigue damage. Performing X-ray CT at multiple stages does not only elucidate the role of multiple defects in crack initiation but also their evolution under fatigue loading [15]. Such considerations can help improve the newly developed smFCG method in predicting the total fatigue life.

In a lab setting, we can easily probe the location of the fracture surface using X-ray CT prior to fatigue testing to gather information on the initial defect population near the critical damage region (see Fig. 4). However, for engineering structures, it is more meaningful to predict the fatigue life before failure. This requires a virtual testing or certification approach. The microstructure in critical regions can be generated virtually in terms of the statistical defect population obtained by X-ray CT. Then various fatigue life prediction methods can be run on virtual specimens to establish a probabilistic fatigue *S–N* (*P–S–N*) curve validated against a small number of HCF experiments.

6. Conclusions

In this work, test campaigns for measuring the uniaxial tensile, fatigue, and fracture mechanics response were undertaken to analyze the fatigue damage and failure behavior caused by the defects in SLM-processed AlSi10Mg alloys. X-ray CT was used to visualize the morphology, size, and location of the initial defects. Within the framework of fracture mechanics, the single crack model and newly developed multiple crack propagation (smFCG) model have been formulated to assess the fatigue cracking process. The FE simulation made it possible to quantify the coupling effect of multiple cracks of the SLM-processed materials. Important conclusions can be drawn as follows:

(1). For these additively manufactured materials cracking tends to be dominated by large LOF defects randomly located near the surface.
(2). For high stress amplitudes, competitive multiple cracking was frequently identified, particularly when multiple defects were located together, or nearly, in the same plane perpendicular to the loading axis.
(3). During the growth of two slightly off-plane cracks, fracture of the bridging ligament occurs when the two cracks start to overlap creating ridges on the fracture surfaces. This is evidenced by a series of ledges on the fracture surface.
(4). A single crack model can effectively predict the evolution of the crack front aspect ratio and the single crack propagation life, which is in good agreement with the *in situ* experimental result when a single crack is dominant. It is non conservative when multiple defects initiate cracks or contribute to the crack surface.
(5). The present smFCG model can depict the growth and merging process of multiple cracks at the fractured surface, leading to a more conservative fatigue crack propagation lifetime estimate compared with the single crack growth model.

Disclosure statement

No potential conflict of interest was reported by any authors when submitting the paper.

Declaration of Competing Interest

The authors declare that they have no known competing financial interests or personal relationships that could have appeared to influence the work reported in this paper.

Acknowledgements

The authors sincerely thank the Joint Fund of Large-scale Scientific Facility of National Natural Science Foundation of China (U2032121). Philip J. Withers also acknowledges the European Research Council grant (CORREL-CT, Grant No. 695638) and EPSRC grant EP/P006566/1. Shengchuan Wu is extremely grateful for the visiting position at the Henry Royce Institute for Advanced Materials (funded through EPSRC grants EP/R00661X/1, EP/S019367/1, EP/P025021/1 and EP/P025498/1).

References

[1] Di Giovanni MT, de Menezes JTO, Bolelli G, Cerri E, Castrodeza EM. Fatigue crack growth behavior of a selective laser melted AlSi10Mg. Eng Fract Mech 2019;217:106564. https://doi.org/10.1016/j.engfracmech.2019.106564.
[2] Thijs L, Kempen K, Kruth J-P, Van Humbeeck J. Fine-structured aluminium products with controllable texture by selective laser melting of pre-alloyed AlSi10Mg powder. Acta Mater 2013;61(5):1809–19.
[3] Zhai Y, Lados DA, LaGoy JL. Additive manufacturing: making imagination the major limitation. JOM 2014;66(5):808–16.
[4] Bao J, Wu S, Withers PJ, Wu Z, Li F, Fu Y, et al. Defect evolution during high temperature tension-tension fatigue of SLM AlSi10Mg alloy by synchrotron tomography. Mater Sci Eng A 2020;792:139809. https://doi.org/10.1016/j.msea.2020.139809.
[5] Kempen K, Thijs L, Van Humbeeck J, Kruth J-P. Processing AlSi10Mg by selective laser melting: parameter optimisation and material characterization. Mater Sci Technol 2015;31(8):917–23.
[6] Gao S, Tan Z, Lan L, He Bo. Effects of geometrical size and structural feature on the shape-distortion behavior of hollow Ti-alloy blade fabricated by additive manufacturing process. J Laser Appl 2020;32(3):032005. https://doi.org/10.2351/7.0000034.
[7] du Plessis A, Beretta S. Killer notches: the effect of as-built surface roughness on fatigue failure in AlSi10Mg produced by laser powder bed fusion. Addit Manuf 2020;35:101424. https://doi.org/10.1016/j.addma.2020.101424.
[8] Laquai R, Müller BR, Kasperovich G, Haubrich J, Requena G, Bruno G. X-ray refraction distinguishes unprocessed powder from empty pores in selective laser melting Ti-6Al-4V. Mater Res Lett 2018;6(2):130–5.
[9] Gu C, Lu Y, Luo AA. Three-dimensional visualization and quantification of microporosity in aluminum castings by X-ray micro-computed tomography. J Mater Sci Technol 2021;65:99–107.
[10] Wu ZK, Wu SC, Zhang J, Song Z, Hu YN, Kang GZ, et al. Defect induced fatigue behaviors of selective laser melted Ti-6Al-4V via synchrotron radiation X-Ray tomography. Acta Metall Sin 2019;55(7):811–20.
[11] Hu YN, Wu SC, Wu ZK, Zhong XL, Ahmed S, Karabal S, et al. A new approach to correlate the defect population with the fatigue life of selective laser melted Ti-6Al-4V alloy. Int J Fatigue 2020;136:105584. https://doi.org/10.1016/j.ijfatigue.2020.105584.
[12] Wang P, Zhou H, Zhang L, Chen H, Zhu X, Lei H, et al. In situ X-ray micro-computed tomography study of the damage evolution of prefabricated through-

holes in SLM-Printed AlSi10Mg alloy under tension. J Alloy Compd 2020;821:153576. https://doi.org/10.1016/j.jallcom.2019.153576.
[13] Domfang Ngnekou JN, Nadot Y, Henaff G, Nicolai J, Kan WH, Cairney JM, et al. Fatigue properties of AlSi10Mg produced by additive layer manufacturing. Int J Fatigue 2019;119:160–72.
[14] Romano S, Brückner-Foit A, Brandão A, Gumpinger J, Ghidini T, Beretta S. Fatigue properties of AlSi10Mg obtained by additive manufacturing: Defect-based modelling and prediction of fatigue strength. Eng Fract Mech 2018;187:165–89.
[15] Tammas-Williams S, Withers PJ, Todd I, Prangnell PB. The influence of porosity on fatigue crack initiation in additively manufactured titanium components. Sci Rep 2017;7(1):7308.
[16] Larrosa NO, Wang W, Read N, Loretto MH, Evans C, Carr J, et al. Linking microstructure and processing defects to mechanical properties of selectively laser melted AlSi10Mg alloy. Theor Appl Fract Mec 2018;98:123–33.
[17] Wu Z, Wu S, Bao J, Qian W, Karabal S, Sun W, et al. The effect of defect population on the anisotropic fatigue resistance of AlSi10Mg alloy fabricated by laser powder bed fusion. Int J Fatigue 2021;151:106317. https://doi.org/10.1016/j.ijfatigue.2021.106317.
[18] Moukawsher EJ, Grandt AF, Neussl MA. Fatigue life of panels with multiple site damage. J Aircraft 1996;33(5):1003–13.
[19] Pang K, Yuan H. Fatigue life assessment of a porous casting nickel-based superalloy based on fracture mechanics methodology. Int J Fatigue 2020;136:105575. https://doi.org/10.1016/j.ijfatigue.2020.105575.
[20] Kamaya M. Growth evaluation of multiple interacting surface cracks. Part I: Experiments and simulation of coalesced crack. Eng Fract Mech 2008;75(6):1336–49.
[21] Chew Y, Pang JHL. Fatigue life prediction model for laser clad AISI 4340 specimens with multiple surface cracks. Int J Fatigue 2016;87:235–44.
[22] Murakami Y, Nemat-Nasser S. Interacting dissimilar semi-elliptical surface flaws under tension and bending. Eng Fract Mech 1982;16(3):373–86.
[23] Sethuraman R, Siva Sankara Reddy G, Thanga Ilango I. Finite element based evaluation of stress intensity factors for interactive semi-elliptic surface cracks. Int J Pres Ves Pip 2003;80(12):843–59.
[24] KISHIMOTO K, SOBOYEJO W, KNOTT J, SMITH R. A numerical investigation of the interaction and coalescence of twin coplanar semi-elliptical fatigue cracks. Int J Fatigue 1989;11(2):91–6.
[25] Maierhofer J, Pippan R, Gänser H-P. Modified NASGRO equation for physically short cracks. Int J Fatigue 2014;59:200–7.
[26] du Plessis A, Yadroitsev I, Yadroitsava I, Le Roux SG. X-ray microcomputed tomography in additive manufacturing: a review of the current technology and applications. 3D Print Addit Manuf 2018;5(3):227–47.
[27] Wang ZY, Wu SC, Kang GZ, Li H, Wu ZK, Fu YN, et al. In-situ synchrotron X-ray tomography investigation on damage mechanism of an extruded magnesium alloy in uniaxial low-cycle fatigue with ratchetting. Acta Mater 2021;211:116881.
[28] Serrano-Munoz I, Buffiere J-Y, Mokso R, Verdu C, Nadot Y. Location, location & size: defects close to surfaces dominate fatigue crack initiation. Sci Rep 2017;7(1):45239.
[29] Uzan NE, Shneck R, Yeheskel O, Frage N. Fatigue of AlSi10Mg specimens fabricated by additive manufacturing selective laser melting (AM-SLM). Mat Sci Eng A 2017;704:229–37.
[30] Hu YN, Wu SC, Withers PJ, Zhang J, Bao HYX, Fu YN, et al. The effect of manufacturing defects on the fatigue life of selective laser melted Ti-6Al-4V structures. Mater Design 2020;192:108708. https://doi.org/10.1016/j.matdes.2020.108708.
[31] Wu SC, Song Z, Kang GZ, Hu YN, Fu YN. The Kitagawa-Takahashi fatigue diagram to hybrid welded AA7050 joints via synchrotron X-ray tomography. Int J Fatigue 2019;125:210–21.
[32] Wu SC, Xu ZW, Kang GZ, He WF. Probabilistic fatigue assessment for high-speed railway axles due to foreign object damages. Int J Fatigue 2018;117:90–100.
[33] Newman J. Fatigue-life prediction methodology using small-crack theory. Int J Fatigue 1999;21(2):109–19.
[34] VANDERWALDE K, BROCKENBROUGH J, CRAIG B, HILLBERRY B. Multiple fatigue crack growth in pre-corroded 2024–T3 aluminum. Int J Fatigue 2005;27(10-12):1509–18.
[35] Seifi R, Ghadimian O, Ranjbaran M. Study on life and path of fatigue cracks in multiple site damage plates. Int J Fatigue 2015;80:449–58.
[36] Li P, Lee PD, Lindley TC, Maijer DM, Davis GR, Elliott JC. X-ray microtomographic characterisation of porosity and its influence on fatigue crack growth. Adv Eng Mater 2006;8(6):476–9.
[37] Shin CS, Cai CQ. Experimental and finite element analyses on stress intensity factors of an elliptical surface crack in a circular shaft under tension and bending. Int J Fract 2004;129(3):239–64.
[38] Iranpour M, Taheri F. A study on crack front shape and the correlation between the stress intensity factors of a pipe subject to bending and a plate subject to tension. Mar struct 2006;19(4):193–216.
[39] Suryawanshi J, Prashanth KG, Scudino S, Eckert J, Prakash Om, Ramamurty U. Simultaneous enhancements of strength and toughness in an Al-12Si alloy synthesized using selective laser melting. Acta Mater 2016;115:285–94.
[40] Lin XB, Smith RA. A numerical simulation of fatigue growth of multiple surface initially semicircular defects under tension. Int J Pres Ves Pip 1995;62(3):281–9.
[41] Pang JHL, Hoh HJ, Tsang KS, Low J, Kong SC, Yuan WG. Fatigue crack propagation analysis for multiple weld toe cracks in cut-out fatigue test specimens from a girth welded pipe. Int J Fatigue 2017;94:158–65.
[42] CARPINTERI A. Shape change of surface cracks in round bars under cyclic axial loading. Int J Fatigue 1993;15(1):21–6.
[43] Lin XB, Smith RA. Shape evolution of surface cracks in fatigued round bars with a semicircular circumferential notch. Int J Fatigue 1999;21(9):965–73.
[44] Biswal R, Zhang X, Shamir M, Al Mamun A, Awd M, Walther F, et al. Interrupted fatigue testing with periodic tomography to monitor porosity defects in wire + arc additive manufactured Ti-6Al-4V. Addit Manuf 2019;28:517–27.
[45] Wu Z. The shape of a surface crack in a plate based on a given stress intensity factor distribution. Int J Pres Ves Pip 2006;83(3):168–80.
[46] Yu PS, Guo WL. An equivalent thickness conception for prediction of surface fatigue crack growth life and shape evolution. Eng Fract Mech 2012;93:65–74.
[47] Chang T, Guo W. A model for the through-thickness fatigue crack closure. Engng Fract Mech 1999;64(1):59–65.
[48] Wu SC, Yu C, Yu PS, Buffière JY, Helfen L, Fu YN. Corner fatigue cracking behavior of hybrid laser AA7020 welds by synchrotron X-ray computed microtomography. Mater Sci Eng A 2016;651:604–14.
[49] Yu PS, Guo W. An equivalent thickness conception for evaluation of corner and surface fatigue crack closure. Eng Fract Mech 2013;99:202–13.
[50] Biswal R, Syed AK, Zhang X. Assessment of the effect of isolated porosity defects on the fatigue performance of additive manufactured titanium alloy. Addit Manuf 2018;23:433–42.